Ground-State Wave Function of Shallow Donors in Uniaxially Stressed Silicon: Piezohyperfine Constants Determined by Electron-Nuclear Double Resonance*

Edward B. Hale† and Theodore G. Castner, Jr.

Department of Physics and Astronomy, University of Rochester, Rochester, New York 14627

(Received 10 October 1969)

Stress-induced changes in the ENDOR spectra of a shallow donor electron interacting with various Si^{29} nuclei neighboring the donor have been experimentally and theoretically investigated. For each of the three measured donors – As, P, and Sb – the compressional, uniaxial stress was applied along the [001] axis and its magnitude corresponded to strains up to 10^{-3}. To describe the observed linear and quadratic shifts and splittings of the lines in an ENDOR shell, we have defined a set of piezohyperfine constants. One piezohyperfine constant was measured for each ⟨111⟩-axis-class shell; three independent piezohyperfine constants were measured for each shell of the other shell symmetry classes. Piezohyperfine constants are reported for more than 15 measured lattice shells about each donor. Analysis of the results shows that the constants for any one shell can be attributed primarily to changes in the Fermi contact hyperfine constants at the various lattice sites within that shell. Consequently, the stress-induced changes are directly related to wave-function density changes at specific points in the lattice. Calculations of these wave-function density changes have been performed using a model based on the valley-repopulation effect and on an effect due to the redistribution of the radial envelope function (RREF effect). The calculations and experimental results are qualitatively in good agreement. The quanitative theoretical accuracy is not sufficient to match all the experimental shells to the actual lattice shells, but a new match of shell Q and the $(1,1,5)$ shell has been determined and other matchings are suggested. The theoretical and experimental results provide information on two intrinsic lattice parameters: the deformation-potential constant Ξ_u, and the location of the conduction-band minimum k_0. Difficulties with assigning a value to Ξ_u because of the RREF effect are discussed. A revised "spin-resonance" value for Ξ_u was found to be 10 ± 1 eV. Applying the above model to the previously matched shells [A and $(0,0,4)$, B and $(4,4,0)$, and K and $(0,0,8)$], one finds an average $k_0 = (0.86 \pm 0.02) k_{max}$.

I. INTRODUCTION

A group-V atom which substitutes at a normal semiconductor lattice site forms one of the best understood impurity centers in solid-state physics.[1] At low temperatures, the center is characterized as an unpaired donor electron which is weakly bound to the impurity atom. This paper is concerned with the ground state of the above configuration when the impurity is either an arsenic, an antimony, or a phosphorus atom in a silicon single crystal.

A sensitive technique, developed by Feher,[2] for studying these impurity centers has been electron-nuclear double resonance (ENDOR). This technique provides detailed information on the hyperfine interaction of the donor electron with numerous Si^{29} nuclei neighboring the donor. The original ENDOR measurements on each of the three donor centers[3] yielded the interaction with about 30 lattice nuclei which composed five different lattice shells. More recent ENDOR measurements of Hale and Mieher[4] yielded the interaction with about 150 lattice nuclei which composed about 15 additional shells. The hyperfine constants determined from these studies provided substantial information on the donor-electron wave-function structure. The isotropic or Fermi contact hyperfine constants yielded the electron wave-function density at the lattice nuclei. The angular-dependent or dipole-dipole hyperfine constants yielded information on the distribution of the wave function about the same nuclei.

Uniaxial stress is another very useful means for experimentally investigating the properties of the donor centers.[5–11] This occurs because the donor wave function is formed from a stress-dependent combination of the crystal band wave functions from each of the various conduction-band valley minima.[12,6] The stress removes the energy degeneracy of these minima[13] and thereby produces two different, but not unrelated, effects on the donor-electron wave function. The first of these is the valley-repopulation effect caused by preference of the electron to be in the lower-energy valleys rather than the higher-energy valleys.[12] The second effect is a change in the one-valley hydrogen-like envelope function caused by stress-induced changes in the donor energy level relative to the valley minimum.[14]

The present study has combined the above two techniques – stress and ENDOR – to further in-

vestigate the properties of the donor impurity centers. (Kohn has mentioned[1] that such an experiment should yield interesting information on changes in the donor-electron wave-function structure.) The primary purpose of this paper is to obtain a better experimental, as well as theoretical, understanding of the effects of uniaxial stress on the wave-function structure of a ground-state donor electron. This paper also presents new information which further improves the understanding of the unstressed electronic structure. In addition, this paper considers the implications of the stressed EPR and ENDOR results in determining the intrinsic silicon lattice value for the location of the conduction-band minimum and one of the deformation potential constants Ξ_u at the minimum.

In a previous study by Wilson and Feher,[6] the effect of stress on the donor-electron spin-resonance spectrum in silicon was reported. Their results for the change in the donor contact hyperfine constant with [001] uniaxial stress showed a decrease which was quadratically dependent on the applied stress. In addition, they reported a stress result for one ENDOR shell (shell B). It had a linear shift with stress. (These quadratic and linear shifts were predicted by Kohn.[1]) The present study reveals for each donor impurity a quadratic change in the Fermi contact constant for five $\langle 111 \rangle$ axis lattice shells or about 20 neighboring nuclei. Furthermore, an initial linear dependence with second-order quadratic effects has been found for the change in the contact constant for about a dozen other shells. To describe the results we have introduced certain parameters which we call piezohyperfine constants. These piezohyperfine constants are distinct for each lattice shell and can be related to stress-induced changes in the electron wave-function density at the various nuclei neighboring the donor. These new constants have been theoretically calculated and a comparison is made with the calculations and experimental results. The results show these constants can be used to identify shells in the same manner as the Fermi contact constants[3,15] and dipole-dipole constants.[16] As a result, further progress has been made in the difficult problem of assigning the shells.

In Sec. II, the theoretical formulation is described. In Sec. III, the experimental apparatus and results are described. Section IV is a comparison of the theoretical and experimental findings.

II. GROUND-STATE ELECTRON

A. Unstressed Wave Function

Kohn and Luttinger have developed the basic formalism for understanding the nature of the shallow donor states.[17] They show that the donor-electron wave function can be expressed as

$$\psi(\vec{r}) = \sum_{j=1}^{6} \alpha_j F_j(\vec{r}) u_{\vec{k}_j}(\vec{r}) e^{i\vec{k}_j \cdot \vec{r}} \quad , \tag{1}$$

where the sum is over the six conduction-band valley minima, $u_{\vec{k}_j}(\vec{r}) e^{i\vec{k}_j \cdot \vec{r}}$ is the Bloch wave at the jth minimum, $F(\vec{r})$ is the hydrogenlike envelope function, and the various α_j are numerical coefficients which determine the appropriate combination of the various valley wave functions. (For the unstressed ground state the α_j's $= 1/\sqrt{6}$.)

The envelope function $F(\vec{r})$ is determined from a derived effective-mass Schrödinger equation in which (a) the kinetic-energy operator includes the anisotropic effective mass; (b) the Coulomb potential is reduced by the static dielectric constant; and (c) the energy eigenvalue is measured relative to the conduction-band minimum. For the ground state, the envelope function has a large amplitude in the central cell. In this cell the above potential is a poor approximation and the actual potential modifies the simple potential eigenvalue by more than 50%. Despite this central cell potential uncertainty, the tail of the envelope function can still be reasonably approximated by use of the quantum defect method whereby $F(\vec{r})$ is determined as a solution of the equation

$$-(\hbar^2 \nabla^2 / 2m^* - e^2/kr) F(\vec{r}) = E_I F(\vec{r}) \quad , \tag{2}$$

where E_I is the experimentally observed ionization energy. Equation (2) is solved as a differential equation rather than eigenvalue equation, but is valid only outside the central cell where the above potential is presumed to be correct. The above solution for $F(\vec{r})$ can be expressed in terms of a Whittaker function and anisotropic mass effects are introduced by use of the so-called "pancake function."[18] Thus, for the z valley,

$$F_z(\vec{r}) = A_n \frac{W_{n,1/2}(2r/n)}{2r/n} \times \frac{\exp[-((x^2+y^2)/n^2 a_t^2 + z^2/n^2 a_l^2)^{1/2}]}{\exp[-r/na^*]} \quad , \tag{3}$$

where A_n is a normalization constant, $W_{n,1/2}(2r/n)$ is the Whittaker function which approaches zero for large r, and n is given by

$$n = (E_0/E_I)^{1/2} \quad , \tag{4}$$

with E_0 the effective-mass energy and E_I the donor ionization energy. The above form for $F(\vec{r})$ is attributed to Kohn by Feher[3] and is discussed in some detail by Hale and Mieher.[15] E_I was obtained from the experimental optical ionization energies and the other parameters in Eq. (3) have been previously determined.[19]

B. Effects of [001] Uniaxial Stress

1. *Basic Considerations*

When stress is applied to the crystal, the interatomic distances are changed. This modifies the crystal potential and thus changes are introduced into the band structure. The energy changes at various points in the Brillouin zone for a given band are described by deformation-potential constants,[20] which are the energy shifts for a unit strain. Two different deformation constants are necessary to describe the energy shift for any one of the six conduction-band minima valleys.[21] However, the dilatational constant shifts every valley equally, hence contributes only to the energy center of gravity shift, and can be neglected in the present calculations. The other constant Ξ_u is positive and produces relative shifts of the six Δ_1 conduction-band minima. A uniaxial compression along a cubic axis lowers the two minima associated with that axis, designated in this paper the z axis, and raises the energy of the four minima perpendicular to the z axis. Consequently, conduction electrons which were originally equally distributed among the six degenerate valleys would thermally repopulate to increase the fraction in the two z valleys. The situation is more complex for the donor ground state because the six valleys are not independent, but strongly coupled.

The valleys are coupled by the short-range potential in the central-cell region. The coupling of the valleys has been treated by the "valley-orbit" matrix approach[12] in which the six basis states are the six different valley wave functions. (Aspects of this approach are given in Appendix C.) The coupling between valleys on different axes has been designated Δ, while that between different valleys on the same axis is represented by $\Delta(1+\delta)$.[22,23] [These energy parameters are not independent (see Ref. 24).] The effect of stress does not couple the valleys. It thus introduces only diagonal terms in the valley-orbit matrix which compete with the off-diagonal short-range potential terms to determine the relative fraction of donor-electron wave function in each valley. A measure of this competition is given by the dimensionless "valley strain parameter" X defined by[6]

$$X \equiv \Xi_u s/6\Delta \quad , \tag{5}$$

where the strain s is proportional to the applied stress – the proportionality constant being an appropriate combination of stiffness coefficients. [For compression both s and X are negative.] When $|X| \sim 1$, the stress terms in the valley-orbit matrix are about equal to the valley coupling terms and substantially modify the wave-function structure and energy of the donor electron. The ground-state energy obtained from a diagonalization of the valley-orbit matrix is[6]

$$E_{gs}(X) = \Delta[-(2+\delta) + \tfrac{1}{2}X - 3(1 + \tfrac{1}{3}X + \tfrac{1}{4}X^2)^{1/2}] , \tag{6}$$

where $E_{gs}(X)$ is measured relative to the center of gravity of the six valleys.

2. *Effect of Valley Repopulation on Wave Function*

The redistribution of the electron among the valleys as the stress is applied means that the α_j coefficients in Eq. (1) are stress dependent. These coefficients have been determined for a [001] stress; the results are[6]

$$\alpha_z = \tfrac{1}{2}[1 - \tfrac{1}{2}(X+\tfrac{2}{3})(1 + \tfrac{1}{3}X + \tfrac{1}{4}X^2)^{-1/2}]^{1/2} \tag{7}$$

and

$$\alpha_x = \alpha_y = \frac{1}{2\sqrt{2}} [1 + \tfrac{1}{2}(X+\tfrac{2}{3})(1 + \tfrac{1}{3}X + \tfrac{1}{4}X^2)^{-1/2}]^{1/2}, \tag{8}$$

where α_z is the coefficient for the two z valleys and α_y is the coefficient for the other four valleys. The valley-repopulation effect on the wave function can thus be determined from Eq. (1) using the coefficients given in Eqs. (7) and (8).

3. *Radial Redistribution Effects on Wave Function*

The wave function may also change due to stress because the Bloch function or the envelope function changes with stress [see Eq. (1)]. In the present experiment for [001] axis stress, no readily apparent changes in the Bloch function have been observed and therefore we assume it does not change with stress. However, for the envelope function, observable changes with stress have been predicted by Fritzsche.[14] These changes occur because the relative energy difference between the donor ionization energy and the valley minimum associated with the $F(\vec{r})$ changes with stress. Thus, the Whittaker function index n as defined by Eq. (4) becomes valley and stress dependent.[25] Using Eq. (4), one obtains

$$n_j(X) = \left(\frac{+E_0}{E_0 + \Lambda + \Delta[(2+\delta) \pm \tfrac{3}{2}X + 3(1 + \tfrac{1}{3}X + \tfrac{1}{4}X^2)^{1/2}]} \right)^{1/2} , \tag{9}$$

where the upper sign is to be used for the two z valleys and the lower sign for the four other valleys. (The values for Λ, Δ, and δ are given in Ref. 22.)

This change in n with stress primarily produces a redistribution of the radial envelope function $F(\vec{r})$ which hereafter will be referred to as the RREF effect. The changes in the radial wave function are different for those envelope functions whose minima are along the stress axis than for those minima perpendicular to the stress axis. Figure 1 illustrates the RREF effect for an arsenic donor. The RREF effect has been calculated and

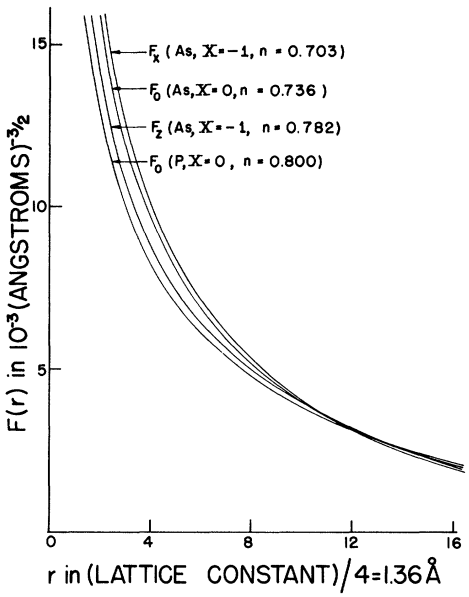

FIG. 1. Stress dependence of the redistribution of the radial envelope function (the RREF effect). The curves shown are for the isotropic Whittaker function and neglect the effect of the pancake factor. The unstressed radial envelope function for every valley (F_0) is the same. The stressed function is different for valleys along the stress axis (F_z) than for those valleys perpendicular to the stress axis ($F_x = F_y$). Note that the radial envelope functions for different donors [F_0 (As) and F_0 (P)] are different because of a difference in ionization energy (i.e., Whittaker function index n).

studied in some detail since its influence is observed in the experimental results.

As the figure shows, when n increases the envelope function becomes less sharply peaked or more diffuse. At $n = 1$, it is an exponential since the energy is then the eigenvalue associated with the uncorrected Coulombic potential. There is a crossover radius at approximately $\frac{3}{4}a^*$ (~16 Å) where the wave function is not altered. Since it is unlikely that shells with a radius much greater than the crossover radius have been measured, the RREF effect as applied to a shell of interest produces a decrease in $F(\vec{r})$ for $\Delta n \equiv n(X) - n(0) > 0$ and an increase in $F(\vec{r})$ for $\Delta n < 0$.

This RREF effect change in the wave function is donor dependent. This donor dependence occurs not because of a different rate of change of $F(\vec{r})$ with n, but because of a different rate of change of n with X, namely, that the chemical shift parameters Δ, δ, and Λ enter directly into Eq. (9). The donor dependence is important and produces observable effects. [Note that the valley repopulation effect depends on only the valley strain and is not donor dependent, see Eqs. (7) and (8).]

C. Hyperfine Interactions

1. *Hyperfine Tensor of a Lattice Nucleus*

A typical hyperfine tensor of interest, $\vec{A}_l$, couples the donor electron spin $\vec{S}$ to a Si^{29} nuclear spin $\vec{I}_l$ where l is an enumeration parameter which corresponds to a lattice site in the neighborhood of the donor. When $\vec{A}_l$ is expressed in terms of the scalar Fermi contact constant a_l and the dipole-dipole tensor $\vec{B}_l$ we have

$$\vec{A}_l = a_l \vec{1} + \vec{B}_l \ , \tag{10}$$

where $$a_l = \tfrac{8}{3}\pi g g_n \beta \beta_n |\psi(\vec{r}_l)|^2 \tag{11}$$

with g, g_n, β, and β_n the electron g factor, the nuclear g factor, the Bohr magneton, and the nuclear magneton, respectively. Thus, a_l is related to the wave-function density at the lth site by known constants. Consequently, measuring the various a_l's is a sensitive means of determining $|\psi|^2$ at various points in the crystal. If $|\psi(\vec{r}_l)|^2$ is determined from Eq. (1) and inserted into Eq. (11), then

$$a_l = A_0[\alpha_x F_x(\vec{r}_l)\cos k_0 x_l + \alpha_y F_y(\vec{r}_l)\cos k_0 y_l + \alpha_z F_z(\vec{r}_l)\cos k_0 z_l]^2, \tag{12}$$

where k_0 is the absolute value of the k vector at any of the six band minima and A_0 is a constant given by $A_0 = \frac{32}{3}\pi g g_n \beta \beta_n |u_{k_0}(r)|^2$, which is independent of site, since $|u_{k_0}(r)|^2$ must be the same at every site.

2. *Nuclei with Equal Fermi Contact Interactions*

a. Unstressed crystal. To specify the nuclei neighboring the donor we introduce a coordinate system centered at the donor atom and locate the nuclei at the lattice sites by coordinate integers. A nearest-neighbor nucleus is assumed at the positive (1, 1, 1) position; a general nucleus is located at the position (n_1, n_2, n_3) where the three n's must be all odd or all even integers. In these length units, the lattice constant is equal to four. Furthermore, we group the nuclei into shells centered on the donor. The equivalent nuclei in a shell are those which transform into each other under the group operators which leave the physical relationship between the donor, the lattice, and any applied perturbation invariant.

For experimental reasons, it is advantageous to subdivide the shells into four distinct symmetry classes depending on the crystallographic locations of the various nuclei in the shell. The shell classes are (a) the unique class in which all the coordinate integers are unique, i.e., $n_1 \neq n_2 \neq n_3$; (b) the {110} plane class in which two of the integers are equal, but nonzero; (c) the ⟨111⟩ axis class in

which all three integers are equal; (d) the ⟨001⟩ axis class in which two of the integers are zero. (The unique class will not be further considered since no experimental shells of this symmetry have been reported.) The number of nuclei in a {110}-plane-class shell is 12. The number in a ⟨111⟩-axis-class shell is four. The number in a ⟨001⟩ axis class is six.

b. Stressed crystal. When stress is applied to the crystal, the equivalence of some of the nuclei in the unstressed shell is removed. The nuclei can be then be grouped into sets. The number of nuclei in all sets must be equal to the number in the unstressed shell class. The number of sets is dependent on the shell class and the stress direction. The sets for a [001] axis stress are discussed below and in Appendix A.

Consider first a {110}-plane-class shell. The 12 shell nuclei are located at the positions (m,n,n), $(m,\bar{n},\bar{n})$, $(\bar{m},\bar{n},n)$, $(\bar{m},n,\bar{n})$, (n,m,n), $(\bar{n},m,\bar{n})$, $(n,\bar{m},\bar{n})$, $(\bar{n},\bar{m},n)$, (n,n,m), $(\bar{n},\bar{n},m)$, $(n,\bar{n},\bar{m})$, and $(\bar{n},n,\bar{m})$. The first group of four sites we call the x sites since the coordinate integer m occurs as the x coordinate; the next group of four are the y sites; and the last group of four are the z sites. For stress along the [001] or z axis it is shown in Appendix A that (a) the four z sites form a set and (b) the x and y sites form another set of eight nuclei. For a ⟨001⟩-axis-class shell, there are two nuclei belonging to each of the x-, the y-, and the z-site categories. Under [001] axis stress, the shell decomposes into two sets just as for the {110} plane class except the number of nuclei per set is reduced by a factor of 2. For a ⟨111⟩-axis-class shell, $m=n$ so there are no distinguishable x-, y-, and z-site categories. The [001] axis stress does not remove the equivalence of the shell nuclei; thus these shells do not decompose into sets.

3. *Stressed Hyperfine Tensors*

Hyperfine tensors for nuclei in the same shell are related. These related tensors have the same Fermi contact term. However, the related dipole-dipole tensors are different, but can be related by a proper permutation and/or sign change of some of the tensor components. In the case of a stress perturbation the new hyperfine tensors for nuclei which form a set are still related.

To compute the stressed hyperfine tensors we first consider the dependence of the Fermi contact constants on a [001] axis stress. We assume stress changes occur only due to the valley-repopulation and RREF effects. We have, using Eq. (12),

$$a(z\text{ sites}) \equiv a_z(X) = A_0\left[\alpha_z F_z(X)\cos\left(\tfrac{1}{2}\pi\frac{k_0 m}{k_{\max}}\right) + 2\alpha_x F_x(X)\cos\left(\tfrac{1}{2}\pi\frac{k_0 n}{k_{\max}}\right)\right]^2 \tag{13}$$

and

$$a(x\text{ sites or }y\text{ sites}) \equiv a_y(X) = A_0\left[\alpha_z F_z(X)\cos\left(\tfrac{1}{2}\pi\frac{k_0 n}{k_{\max}}\right) + \alpha_x F_x(X) \times\left\{\cos\left(\tfrac{1}{2}\pi\frac{k_0 n}{k_{\max}}\right) + \cos\left(\tfrac{1}{2}\pi\frac{k_0 m}{k_{\max}}\right)\right\}\right]^2, \tag{14}$$

where $k_{\max} = 2\pi/(\text{lattice constant})$ and the stress dependence of F_j is accounted for by the stress dependence of n_j as given in Eq. (9). A quantity easily obtained from the data is a parameter Δa, which we call the piezohyperfine splitting parameter. It is given by

$$\Delta a \equiv \tfrac{1}{2}[a_z(X) - a_y(X)] \ . \tag{15}$$

We have studied the features of Eqs. (13)–(15) in detail and have also programmed them on a computer. The findings from the Δa_y or Δa_z studies show that for shells of greatest interest (radius < 15 Å) the RREF effect competes with the valley-repopulation effect and reduces the effect of the stress. Namely, as the energy increases (decreases), the valley population decreases (increases), and the envelope function becomes more (less) localized. For $|X| \lesssim \frac{1}{2}$ and $r \sim 8$ Å, the change in the $\alpha_j F_j$ product due to the RREF effect is about $-\frac{1}{5}$ the change due to the valley-repopulation effect for the z valleys and about twice as large for the x or y valleys. Calculations valid for small values of X are considered in Appendix B. More detailed results are discussed in Sec. IV.

Stress-induced changes are also expected for the components of the dipole-dipole tensor, namely, B_{zz}, B_{xy}, and B_{xz} [referred to the cubic axes of Si for the (n,n,m) site]. The unstressed hyperfine components have recently been calculated by Hale and Mieher.[16] They found the components could be expressed in a form somewhat similar to Eq. (12) involving cosine terms (with different phases for some components), however, with A_0 being replaced by an integral of the product of two periodic band functions and a magnetic dipole operator. Their results indicated B_{zz} could be expressed as a single term with a single integral I_0, while B_{xy} and B_{xz} involved two terms with two different constants. For the magnetic field along the [100] axis only the B_{zz} component contributes in first order to the ENDOR transition frequency. (For the field along the [110] axis B_{xy} will also contribute in first order.) If stress-induced changes in the dipolar integrals can be neglected [i.e., $u_{\vec{k}}(\vec{r})$ changes with stress are negligible], then the changes in the dipolar hyperfine constants are due to valley-repopulation and the RREF effect. An explicit calculation, based only on valley repopulation, of the quantity B_{zz} (z sites) $-$ B_{zz} (y sites) yields a term linear in the valley strain which contains cosine

terms. The ratio of this splitting to $a_z(X)$-$a_y(X)$ is proportional to the quantity (I_0/A_0), which from the zero stress data for shells A and B is known to be about $\frac{1}{20}$. The calculation indicates the linear splitting due to this dipolar contribution is less than 10% of Δa for most shells, with a few exceptions.[26] This means that [001] axis stress-induced changes in the dipolar constants are expected to be unobservable or marginally observable for most shells, within the limitations of the present experiment. For this reason, changes in the dipolar constants have not been calculated in detail in this paper.

III. EXPERIMENTAL DETAILS AND RESULTS

A. Apparatus

The samples were cut from single-crystal ingots which were nominally doped to about 8×10^{16} donors/cm^3. They were rectangular parallelepipeds $\frac{1}{4}\times\frac{1}{4}\times\frac{3}{4}$ in. with the uniaxial stress applied along the long dimension. The samples were ground using a precision surface grinder. The surface to be ground was oriented to be a principal plane of the crystal by use of a x-ray diffraction unit. This unit is mounted on one end of a Do-All grinder so that the sample was not demounted between orienting and grinding of each surface. From the estimated accuracy of the instruments and the parallelism of the final surfaces, each surface was within 3 min of being parallel to the desired crystal plane.

Measurements were made using a conventional X-band microwave spectrometer with balanced bolometer detection and 100-cps field modulation. The microwave cavity was modeled after one designed by Castner and Doyle[27] with several modifications as discussed below. The inside cavity dimensions were changed to $0.900\times0.750\times1.600$ in. to take into account the dielectric constant of silicon. The ENDOR coil consisted of 11 turns of 0.010-in.-diam wire. Square holes were cut in the top and bottom of the cavity to permit application of the stress to the sample [see Fig. 2].

The stress was applied to the sample using a vise type of jig shown in Fig. 2. The uniaxial compression is increased by tightening one of the screws with a screw driver of special design. This screw driver consisted of a 3-ft-long stainless-steel tube which extended up the helium Dewar and thru an O-ring joint at the top flange. Soldered to the bottom of the tube was a hexagonal wrench which fit into the Allen head screw of the stress jig. Rotation of the screw driver by a handle outside the Dewar permitted a continuous variation of the stress. In addition, raising or lowering of the screw driver permitted engagement or disengagement of the wrench into the screw head. This adjustment was occasionally made to reduce microphonics and thermal losses. The sample arm of the stress jig contained two $\frac{1}{4}$-in.-diam bronze balls which formed "flexi-ball joints." This flexible degree of freedom in each vise jaw was quite important. It permitted a good mating of the jaw to the sample end surface which greatly improved the homogeneity of the stress within the sample. The broadening of the ENDOR lines with stress gave an indication of the stress uniformity which was 10% or less.

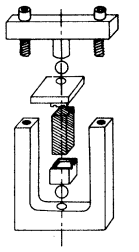

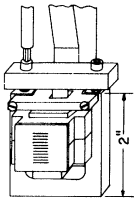

FIG. 2. Design of apparatus to apply stress, ENDOR rf field, microwave field, and dc magnetic field to the sample near liquid-helium temperature. (A) The stress jig transfers the stress through the flexible ball joints to the cross-hatched sample. (B) The jig is mounted to the wave guide such that the sample sits inside the 11-turn ENDOR coil as well as the microwave cavity. For measurements the cavity is located in a Dewar between the pole faces of the dc magnet.

B. Procedures

All measurements were made sitting on top of the bell-shaped, dispersion derivative, lowest-field donor hyperfine line. As the rf oscillator was swept, the ENDOR signals were seen as decreases in the EPR signal. Maximum ENDOR signals were seen near 4 °K in Sb-doped samples and near 6 °K in P-doped samples. The signals from the As-doped samples were obtained at pumped hydrogen temperature ~10 °K. The unstressed line shape and spectra were effectively identical to that seen by Hale and Mieher.[4] The typical measurement procedure consisted of aligning the external magnetic field along the crystal [100] axis and sweeping the entire high-frequency side of the ENDOR spectrum. The [001] axis stress was then changed – usually in increments of about -0.03 valley strain units for $|X|<0.1$ and in increments of about -0.05 valley strain units for other X values – and the new spectrum taken. For $X\approx-\frac{3}{4}$ most of the lines had become so broad that they were no longer detectable. Then the stress was reduced to zero, the magnetic field was ro-

tated to the crystal [110] axis, and the above procedure repeated. Since stress-induced changes in the angularly dependent (dipole-dipole) hyperfine constants were not observed (shell F being an exception), angular rotation studies were, in principle, not necessary. However, the data along the [110] axis was taken as a double check on the [100] axis results, and also to help verify the proper untangling of the various lines when they strongly overlapped as in the clusters.

C. Results

1. *Brief Review of Unstressed Experimental Results*

In previous experiments,[3,4] each shell was assigned an alphabet letter and the symmetry class of the shell was determined by the pattern of the angular rotation spectra. It was found that shells A and K belonged to the ⟨001⟩ axis class; shells C, E, H, J, N, and O belonged to the ⟨111⟩ axis class; shells B, D, F, G, I, L, M, P, Q, R, S, T, V, and X belonged to the {110} plane class.

2. *General Observations under Stress*

As the [001] axis stress is applied, the shifting of many ENDOR lines is readily discernible. Most of the lines shifted by several linewidths. For a given line the shift was found to be independent of the magnetic field direction in the (001) plane if the unstressed angular dependence of the line was allowed for. These results indicate that the dipole-dipole interactions are independent of stress.[28] In addition, for any one shell, it was found that all the x- and y-site lines shifted the same amount while the z-site lines shifted a different amount. [An exception is shell F (see Sec. III C 5).] This is particularly striking for the magnetic field along the [100] axis since for this geometry a line splitting is observed. Figure 3 shows this result for shell B(Sb). For zero stress, the x-axis magnetic field removes the equivalence of the x sites from the equivalence of the y sites and z sites. Thus, two lines are seen. The x-site line (the lower-frequency line in Fig. 3) has one-half the intensity of the y- and z-site degenerate line. When the z-axis stress is applied, it removes the equivalence of the y and the z sites. Thus, the degenerate line splits into two lines of equal intensity. Usually one of the split-off lines increases in frequency while the other split-off line decreases in frequency. Which of the split-off lines belongs to the y sites is determined by observing the shift of the x-sites line, since this line shifts the same amount. In Fig. 3, the y-site line is the low-frequency split-off line.

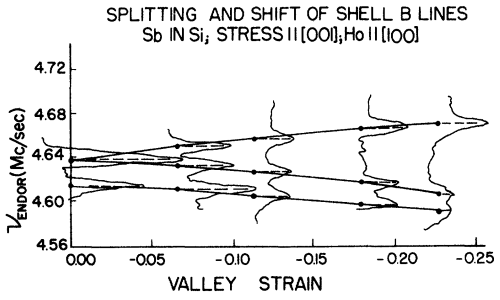

FIG. 3. Effect of stress on the shell B(Sb) ENDOR spectrum. The splitting of the y- and z-site line can be seen as well as the parallel shift of the x- and y-site lines. (The slight convergence of these lines at $X=-0.23$ is attributed to the smaller signal-to-noise ratio and line broadening which produces an overlap of the lines.)

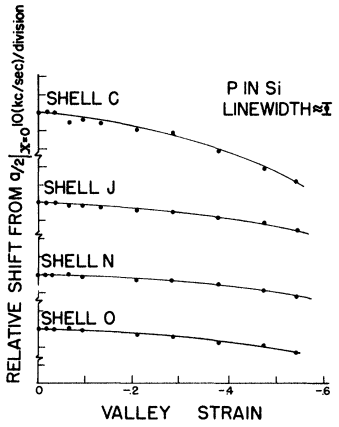

FIG. 4. Quadratic shift of ⟨111⟩-axis-class phosphorus shells.

The magnitude of the splitting of the y- and z-sites line for a typical shell we refer to as the piezohyperfine splitting parameter Δa. We define it to be positive when the z-site high-frequency line occurs at a higher frequency than the y-sites line as in Fig. 3. Since Δa is independent of the magnitude of the magnetic field, independent of the microwave frequency, and directly measurable without corrections from the recording tracings, it is an important experimental parameter.

For ⟨111⟩ axis class of shells, the observed stress behavior is not the same as for the other shell classes. No splitting is observed. Shifts corresponding to decreases in the ENDOR frequencies with applied stress are observed for all the high-frequency ENDOR lines. Again the angular dependence shows the experimentally observed dipolar constants to be independent of stress. Figure 4 shows the results for several ⟨111⟩-axis-class shells for a phosphorus donor.

3. *Calibration of Strain*

The strain has been measured only in terms of the dimensionless valley strain parameter X. An absolute strain determination was not necessary since previous experiments by Wilson and Feher[6] carefully established the relationship between the magnitude of the applied stress and the separation of the donor hyperfine lines from which X can, in principle (see below), be obtained. [Note that X is a "strain unit" of importance since many of the relevant expressions use X as the only strain and donor dependent variable, see, e.g., Eqs. (7), (8), and (20)–(22).]

To establish a relative scale for X is not a difficult problem. This occurs because the Δa splitting parameter for every shell varied linearly with stress despite the fact that (a) the various lines between which Δa is measured often showed large quadratic variations with stress and (b) the various shell values for the Δa's varied over more than an order of magnitude and had both plus and minus values. This linear splitting is clearly shown in Fig. 5 for $\{110\}$ plane class of shells about an arsenic donor. The linear dependence was originally established using the following procedure: The measured Δa values for one shell (such as shell F or shell Q) were plotted on the vertical axis and the horizontal axis coordinate values (strain settings) were chosen so as to obtain a linear plot. For $|X| > 0.2$, measurement of the quadratic donor hyperfine separation verified that the horizontal axis was linear in X. In addition, the fact that the increments between strain settings

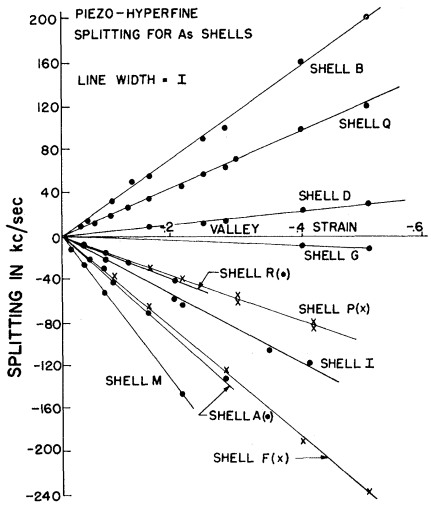

FIG. 5. Piezo-hyperfine splittings at various strain settings for arsenic shells. The splitting is linear with stress and positive if the z-site line has a higher frequency than the x- or y-site line for the high-frequency ENDOR line.

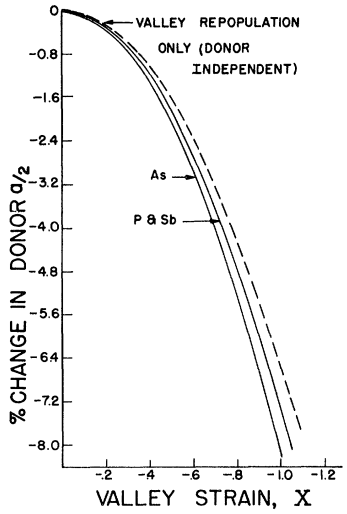

FIG. 6. Model-dependent "calibration" of the valley strain. The dashed line is for the valley-repopulation-only model as used in Ref. 6. The solid curves include the RREF effect with a variable Whittaker function index. (The RREF effect with a variable Bohr radius could not be shown with clarity, but is discussed in the text.)

were roughly equal strongly supports the belief in the linearity of this axis since the stress was applied by nearly equal angular incremental rotations of the strain vise screw. Furthermore, using these now determined strain setting values where all the other Δa's were measured, one finds that the values for any other shell, without exception, lay on a straight line (see Fig. 5). Finally, when the shifts of the line from any one of the $\langle 111\rangle$-axis-class shells is plotted, they show a quadratic strain dependence as expected (see Fig. 4). Thus, several methods have verified the relative scale for X.

To calibrate absolutely the horizontal axis scale in units of X is a considerably more complex problem. One aspect of the problem is concerned with the correct "spin-resonance value" for the deformation potential Ξ_u. In a previous experiment,[6] a quadratic dependence of the donor Fermi contact constant on applied stress was found. The results, which were interpreted using only the valley repopulation effect, gave the values for $6\Delta/\Xi_u$ as 1.32×10^{-3}, 1.98×10^{-3}, and 1.10×10^{-3} for P, As, and Sb donors, respectively. A more recent experiment[23] has measured 6Δ by optical means to be 12.95, 22.4,[29] and 12.14 MeV in the same order of donor atom as above and for $T = 30$ °K. This implies Ξ_u is 9.8, 11.3, and 11.0 eV, respectively. This result is somewhat surprising since Ξ_u is an intrinsic lattice parameter and thus should be independent of donor. We believe at least some of this anomalous donor dependence oc-

curs because the RREF effect has not been included in the above analysis.

Figure 6 shows the theoretical change in the donor contact interaction as a function of valley strain. The dashed curve was calculated using only the valley-repopulation effect which is not donor dependent.[6] The other curves show the results when the RREF effect was included in the calculations.[30] A very important result is that the the shape of all the curves is quite similar. In fact, if the dashed curve is redrawn on the same figure using a stress axis calibration which is reduced 11%, it would be essentially indistinguishable from the As curve. The same is true for a 6% reduction in the case of P and Sb. If the shape of the solid curves were significantly different from the dashed curve, then the Wilson-Feher experiment[6] could, perhaps, have been definitive in establishing the relative importance of the valley-repopulation and the RREF effects at the donor. Clearly, however this is not the case. We have also considered the RREF effect using the calculational procedure of Fritzsche.[14,25] The results are similar to the present method in the shape of the curve and the donor dependence. However, they are about a factor of 4 smaller and require only a 3% correction for an arsenic donor. In summary, it seems that there is a "theoretical uncertainty" of the order of 10% in calibrating the absolute valley strain.

In the present experiment, we have calibrated all our strains for $|X| > \frac{1}{4}$ using the solid curves in Fig. 6. (This is equivalent to a 11% reduction in the valley strain for an As donor and a 6% reduction for P or Sb donors compared with values based on just the valley-repopulation model.) There are two reasons for doing this in addition to using the same form of calculation at every lattice site. First, it improves somewhat the anomalous donor dependence in Ξ_u so that the new values are 9.2, 10.1, and 10.3 eV compared with the previously mentioned values of 9.8, 11.3, and 11.0 eV. Second, these new Ξ_u values are in better agreement with other reported values which are 7.7,[31] (8.3 ± 0.3),[32] (11.3 ± 1.3),[33] 9.57,[34] (8.6 ± 0.2)[35] (at 80 °K, and 7.9 eV[11] for P and Sb in Si or 7.1 for Bi in Si.

4. *Analysis of Data*

The measured line shifts were empirically fit to expressions of the form

$$\Delta a_y = -e_y X - f_y X^2 \ , \tag{16}$$

$$\Delta a_z = -e_z X - f_z X^2 \ , \tag{17}$$

and $$\Delta a = \Delta a_z - \Delta a_y = -eX \ , \tag{18}$$

where Δa_y and Δa_z are the observed shifts of the y sites and z sites, respectively, and Δa is the hyperfine splitting parameter. The e's are constants chosen to describe the linear terms; the f's describe the quadratic terms. For $|X| < \frac{1}{2}$ and within the limits of experimental error,

$$e_x \approx e_y \ , \tag{19a}$$

$$e = e_z - e_x \ , \tag{19b}$$

and $$f_x = f_y = f_z = f \ . \tag{19c}$$

Cubic and higher-order shifts with stress were not directly observable, but their effects may influence the fit to the data. The line shifts were fit in the following manner. The e's were fit effectively in

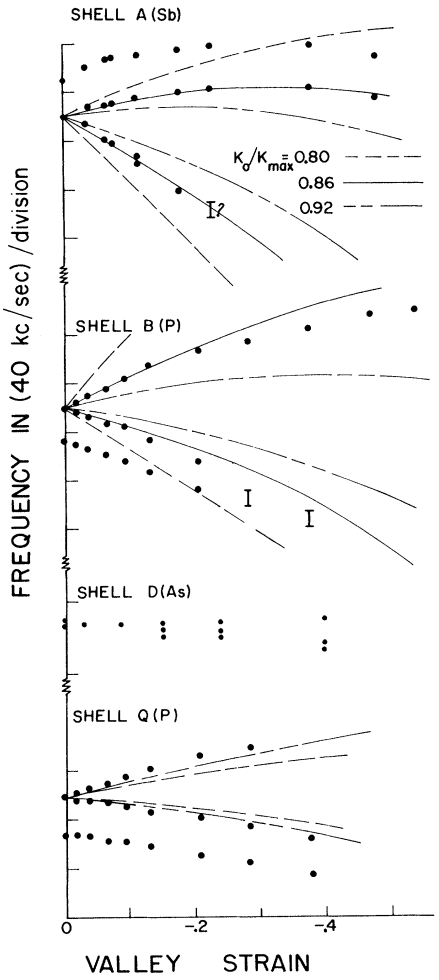

FIG. 7. Shifts and splittings for several shells with $H_0 \| [100]$. Note that the lines shifting at the greatest rate (low-frequency lines for shell A and shell B) can not be followed out to large stress values because of line broadening. The theoretical curves assume shell A is the (0, 0, 4) shell, shell B is the (4, 4, 0) shell, and shell Q is the (1, 1, 5) shell and are for various values of k_0/k_{max} as shown. (The theory curve for the parallel shifting line has not been drawn on the figures.)

TABLE I. Measured piezohyperfine constants.

Shell	Donor	e (kHz)	Error in e (%)	e_y[a] (kHz)	e_g[a] (kHz)	f (kHz)	Error in f (%)	id $\frac{2e}{a_0}$[b]	$\frac{2f}{a_0}$[b]
	As	−495	±5	170	−320	350	±20	−0.129	0.091
A	P	−530	±5	150	−380	320	±20	−0.178	0.107
	Sb	−450	±5	125	−320	210	±20	−0.143	0.068
	As	375	±5	−200	175	250	±30	0.124	0.083
B	P	450	±5	−180	275	220	±20	0.199	0.098
	Sb	270	±5	−135	135	125	±20	0.147	0.068
	As	0	•••	0	0	140	±10	0	0.069
C	P	0	•••	0	0	125	±10	0	0.076
	Sb	0	•••	0	0	92	±10	0	0.066
	As	57	±5	−45	15	30	±30	0.044	0.023
D	P	42	±5	−40	0	60	±20	0.038	0.054
	Sb	63	±5	−40	25	55	±20	0.064	0.055
	As	−470	±5	150	−320	50	±30	−0.418	0.045
F	P	−410	±5	130	−280	80	±20	−0.488	0.095
	As	−24	±10	0	−25	45	±20	−0.030	0.056
G	P	−18	±10	−10	−25	40	±20	−0.024	0.052
	Sb	−36	±10	0	−35	40	±20	−0.048	0.052
	As	0	•••	0	0	65	±20	0	0.081
H	P	0	•••	0	0	45	±20	0	0.065
	Sb	0	•••	0	0	55	±15	0	0.079
	As	−290	±5	65	−230	<25	•••	−0.406	<0.035
I	P	−235	±25	75	−155	55	±20	−0.340	0.080
	Sb	−160	±25	40	−120	40	±20	−0.248	0.062
	As	0	•••	0	0	30	±30	0	0.042
J	P	0	•••	0	0	50	±20	0	0.070
	Sb	0	•••	0	0	45	±15	0	0.071
	As	−385	±40	135	•••	<25	•••	−0.506	<0.035
K	P	−450	±10	155	−295	•••	•••	−0.681	•••
	As	−440?	±10	200	−230?	<25	•••	−0.594	<0.035
L	P	−700	±10	240	−460	•••	•••	−1.203	•••
	As	−740	±10	250	−495	<25	•••	−0.949	<0.035
M	P	−740	±25	280	−460	•••	•••	−1.210	•••
	Sb	−440	±10	190	−250	<25	•••	−0.797	<0.035
	As	0	•••	0	0	30	±15	0	0.048
N	P	0	•••	0	0	35	±20	0	0.056
	As	0	•••	0	0	75	±35	0	0.101
O	P	0	•••	0	0	45	±20	0	0.075
	Sb	0	•••	0	0	60	±20	0	0.088
	As	−195	±5	50	−150	50	±20	−0.280	0.072
P	P	−210	±5	75	−140	90	±20	−0.330	0.13
	Sb	−150	±5	25	−120	55	±20	−0.235	0.09
	As	240	±10	−90	155	<25	•••	0.428	<0.045
Q	P	250	±5	−95	160	•••	•••	0.486	•••
	Sb	220	±10	−95	130	•••	•••	0.576	•••
	As	−210	±5	70	−135	<25	•••	−0.488	<0.06
R	P	−250	±10	130	−120	•••	•••	−0.672	•••
	Sb	−170	±10	65	−100	•••	•••	−0.511	•••
S	P	<|10|	•••	•••	•••	•••	•••	0.02	•••
T	P	<|5|	•••	•••	•••	•••	•••	0.01	•••
U	P	−39	±10	20	−20	40	±20	−0.102	0.10

TABLE I. (*Continued*).

Shell	Donor	e (kHz)	Error in e (%)	e_y [a] (kHz)	e_z [a] (kHz)	f (kHz)	Error in f (%)	id $\frac{2e}{a_0}$ [b]	$\frac{2f}{a_0}$ [b]
V	Sb	−310	±5	115	−190	70	±30	−0.610	0.14
	P	<0	···	50	···	···	···	0	···
X	Sb	<0	···	40	···	45	±20	0	0.10

[a]The error limits for e_y and e_z are somewhat larger than for e.

[b]The $\frac{1}{2}a_0$ values are taken from Ref. 4.

the range $X=0$ to $X\approx-\frac{1}{5}$, i.e., to the initial slope of the $\frac{1}{2}a$-versus-X curve. The f's were then determined as the best-fit value to describe the observed line. The line which occurred at the highest frequency of the two lines was always found to have a positive f value. Furthermore, the splitting parameter was found to have no quadratic shift throughout the measureable range of X values. [This result is the reason for Eq. (19c).] The f value for the lowest-frequency line can be determined from Eq. (19c). In general, it is experimentally difficult to get an accurate quadratic fit for the lower line, since it shifts so much with stress that it readily broadens due to stress inhomogeneities. In this regard, it should be mentioned that most of the data was taken in the range $0>X>-\frac{1}{2}$, not because greater stress could not be applied, but because the lines deteriorate due to stress inhomogeneity broadening. For example, a ±10% inhomogeneity at $X=-\frac{1}{2}$ means a line shifting 200 (kc/sec)/(unit strain) becomes distributed over a 20-kc/sec range or approximately four unstressed linewidths broad. Definite broadening effects are clearly visible in Fig. 3. Note how the linewidth of the high-frequency line is hardly effected at $X=-\frac{1}{4}$ since this line is actually shifting less with stress than at $X=0$ because the negative shift of the quadratic term is observably influencing the shift. However, this negative-shift influence on the lower-frequency line adds to the line broadening. In general, the higher-frequency lines could be observed over a considerably greater range of X values. Some of these features can be seen in Fig. 7.

The measured values for the piezohyperfine parameters e, e_y, e_z, and f are given in Table I for ⟨001⟩-axis-class shells and {110}-plane-class shells. The number of independent experimental parameters for each shell is three – two e values and one f value – since the parameters are related by Eq. (19). Results for the ⟨111⟩-axis-class shells are also reported in Table I. However, in this class there is only one independent piezohyperfine parameter for each shell – one f value – since all the e values are effectively zero. These tables also include the values for id $\equiv 2e/a_0$ and $2f/a_0$. These values we call the (shell) normalized parameters. The normalized parameters are important because they are dimensionless and they can be directly related to percent changes in the wave-function density. For example, $2e_y/a_0$ is the percent linear change in $|\psi|^2$ at the y sites for a unit valley strain. Thus, these normalized parameters can be conveniently compared with the percent wave-function density changes computed theoretically.

5. *Detailed Comments on Results*

The hyperfine parameters for the shells A, B, C, D, F, G, Q, R, and V could be readily determined since their shifting lines were seldom, if ever, obscured by other lines in the spectrum. Figure 7 shows the data points corresponding to line shifts for some of these shells. The lines for the shells H, J, N, and O were often obscured by other lines at small X values. However, the quadratic shifts of these ⟨111⟩-axis-class shell lines become more distinct at larger X values than many lines of the other shells which broaden at a greater rate. The lines of the shells I, K, L, M, and P are rather badly intermixed in the cluster region of the spectrum. Figure 8 shows the phosphorus cluster spectra for several different stresses. Using a plot of the type in Fig. 7, a detailed analysis showed that the line shifts could normally be determined. This analysis permitted the assignment of the lines as shown in Fig. 8. In some cases, considerable difficulties occurred in interpreting the data. The large errors for shell I(P), shell I(Sb), and shell M(P) are a result of these difficulties. In addition, error limits could only be set on the shift of the z-site line for both shell K(As) and L(As). Shell L(Sb) could not be resolved because of entanglement with lines from the region AAA(Sb). The lines of shells S, T, and U form another cluster of intermixed lines. Shells S and T did not have large shifts in either the P or As spectrum. However, shell S(Sb) probably has Δa/(unit valley strain) ~ − 500 kc/sec. Shell X(As) was not well resolved; the z-site line for both shells X(P) and X(Sb) was obscured by lines from other shells. Unfortunately, the line shifts for

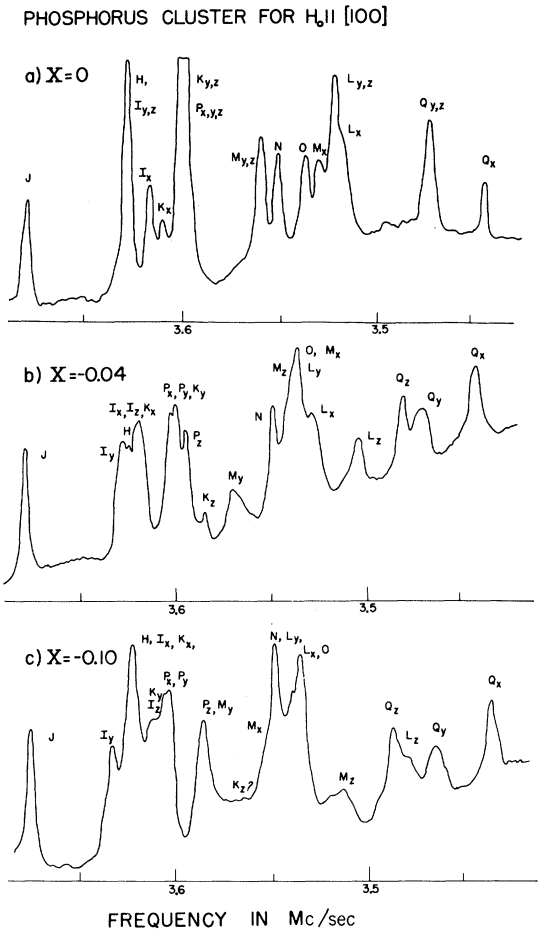

FIG. 8. Phosphorus-doped silicon cluster spectra for several stress values. The line shifts can be determined for most of the lines from analysis of plots similar to those shown in Fig. 7. (Note the sweep rate for each run was slightly different.)

shell E could not be determined. For the present geometry, the lines from shell E(P) and E(Sb) never emerged from the cluster and were obscured because of their weak intensity. For shell E(As) a weak line (corresponding to one lattice site per shell) emerges from the cluster but is difficult to detect even in the unstressed spectrum.

A careful perusal of the data presented in Table I reveals a definite tendency for many of the phosphorous shell id parameters to be relatively too large – the best examples being shells A, B, M, P, and R. A likely explanation is that the absolute valley strain calibration for this donor differs by about 10% from the other donor values as suggested by the 10% donor dependence of the new spin-resonance Ξ_u value [see Sec. III C 3].[36]

The largest dipolar hyperfine constant measured in this experiment is B_{zz} of shell F(As). The stressed spectra along [100] showed that the x-site line and the y-site line for this shell did not shift precisely the same amount. The line separation was 114 ± 2 kc/sec at $X = 0$ and 103 ± 3 kc/sec at $X = -0.40$ and within the rather large experimental uncertainty was linear with stress. This 10% decrease is interpreted as a change in B_{zz}. For shell F(P), there was a (4 ± 2)% decrease in B_{zz} for $X = -\frac{1}{2}$. Other shell B_{zz}, B_{xy} or B_{xz} changes were not studied in detail, but line separation changes greater than 10 kc/sec would have been noticed.

A linear shift of $\Delta|\psi|^2/|\psi|^2 = (60 \pm 5)s$ has previously been reported for shell B(P) for a [100] axis stress.[6] The present measurement is in excellent agreement with this value if it is assumed that the shift with a x-axis strain is for a y- or z-site shift.

The present experiment has determined results relevant to the unstressed data which however cannot be determined directly from the unstressed spectra. One result is that a ⟨111⟩-axis-class shell – which we designate as shell J(Sb) – was buried in the shell P(Sb) spectra. This possibility was not excluded in the unstressed experiment.[4] Shell J(Sb) has $\frac{1}{2}a = 629$ kc/sec and $B_{xy} = 5$ kc/sec. We have confirmed that shell J(As) was intermixed with shell P(As), as was previously suggested, and we have determined its $B_{xy} = 5$ kc/sec. The discrepancy over whether shell D(Sb) was a ⟨111⟩-axis-class shell[3] or whether it was an unresolved {110}-plane-class shell[4] has been absolutely established as the latter since its id $\neq 0$. The possibility that shell S(Sb) and shell S(As) or shell S(P) are from the same lattice shell is now in doubt because of the large id parameter of shell S(Sb). Similar arguments are not out of the question for the L-shell assignments.

Finally, we mention that preliminary results for stresses along other directions have been taken. Additional effects other than those reported here occur because of the shear component in the stress. These will be reported in a future paper.

6. *Errors*

The measurements consisted of measuring the strain, locating the frequency of the line peaks on the recorder tracings, and determining which lines belonged to which shell. The errors involved with measuring the strain have been discussed in Sec. III C 3 and are essentially of a theoretical nature. This theoretical uncertainty has not been considered in the errors given in Table I. The errors in this table are estimates based primarily on locating the centers of the lines. The location of the lines at large stress values is very important in obtaining the best fit to the data. However, at these large stress values the relative errors are greatest

since the lines have broadened and tend to disappear into the spectrometer noise. Once the center of a line is located very little error occurs in determining its frequency since various frequencies are accurately marked on the recorder tracing every 10 kc/sec. The largest errors, as well as some omission of data from Table I, occur because lines strongly overlapped with lines from other shells.

IV. COMPARISON OF THEORETICAL AND EXPERIMENTAL RESULTS

A. Qualitative Agreement

There is good qualitative agreement between the theoretical and experimental results. To consider this qualitative agreement we will use the simple results obtained in Appendix B which are valid for small X and neglect the RREF effect. Equations (B8)–(B10) yield, when expressed in terms of an identifier parameter id which is distinct for each shell,

$$\frac{2\Delta a_z}{a_0} = \frac{\Delta|\psi(n,n,m;X)|^2}{|\psi(n,n,m;0)|^2}$$

$$= -\tfrac{2}{3}X\,\mathrm{id}\left[1-\tfrac{1}{2}X\left(\frac{2(\mathrm{id})^2+2\mathrm{id}-1}{\mathrm{id}}\right)\right], \quad (20)$$

$$\frac{2\Delta a_y}{a_0} = \frac{\Delta|\psi(n,m,n;X)|^2}{|\psi(n,m,n;0|^2}$$

$$= \tfrac{1}{3}X\,\mathrm{id}\left[1-\tfrac{1}{2}X\left(\frac{2+2\mathrm{id}-(\mathrm{id})^2}{\mathrm{id}}\right)\right], \quad (21)$$

and $$2\Delta a/a_0 = -X\,\mathrm{id}[1-\tfrac{1}{12}X(\mathrm{id}+2)] \ . \quad (22)$$

This useful id parameter is given by

$$\mathrm{id} \equiv (1-R)/(1+2R) \ , \quad (23)$$

where

$$R = F_y(\vec{\mathbf{r}})\cos\left(\frac{\pi k_0 n}{2k_{\max}}\right)\Big/F_z(\vec{\mathbf{r}})\cos\left(\frac{\pi k_0 m}{2k_{\max}}\right)$$

and is the site location parameter (see Appendix B). A plot of Eqs. (20) and (21) versus X for various id values is shown in Fig. 9. As discussed below, the experimental results are in good agreement with the shape of these curves.

The simple theoretical expression for the id parameter in Eq. (23) can explain various characteristics seen in the tabulated results of Table I for the many measured id values. It predicts that the donor dependence for the same shell should be negligible; but that the shell dependence for the same donor can be large. It predicts that the value of the measured id parameters will not be large since the measured shells have a large $a_0\alpha(1+2R)^2$ so id $\alpha(1+2R)^{-1}$ will be small [i.e., those shells having $R\sim-\frac{1}{2}$ will not be seen]. In addition, although

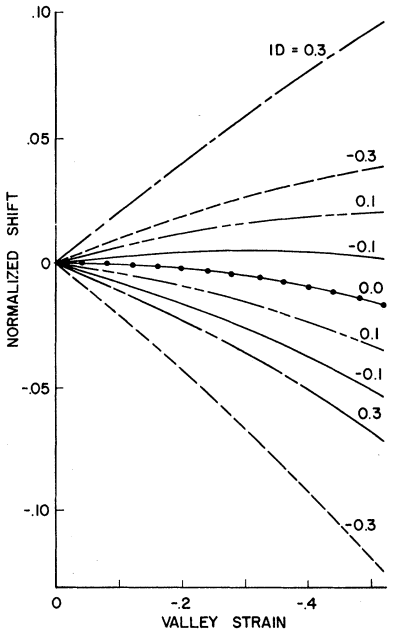

FIG. 9. Universal curve shapes obtained from Eqs. (20) and (21) using the simplified model discussed in Appendix B. For the range of id values shown, the nonlinear terms shift the curves to lower values. The separation between the two branches for the same id value are effectively linear with the stress. For id = 0, the two branches are degenerate as represented by the dots on the curve.

the id parameter may take on both positive ($1>R>-\frac{1}{2}$) and negative values ($R<-\frac{1}{2}$ or $R>1$), more shells with negative id parameters will be seen since their large a_0 values imply large $|R|$ values or id < 0.

Equations (20)–(22) can qualitatively account for the observed shifts and splitting with stress. First, consider the case id = 0 (the ⟨111⟩-axis-class shells being examples). Equation (22) predicts no splitting. Equations (20) and (21) predict no linear shift but quadratic shifts (see also Fig. 9). These predictions are in agreement with our observations (see Fig. 4). For id ≠ 0, linear terms become important. In the present experiment the linear term obscures the quadratic term for $|\mathrm{id}|>\frac{1}{2}$ since the rapidly shifting lines broaden at rather small stress values ($X\approx-\frac{1}{5}$ or smaller). The smaller the id parameter the more observable the quadratic shifts become as can be seen in Fig. 9. For $0<\mathrm{id}<\frac{1}{3}$ the quadratic shift for compression ($X<0$) is negative for the higher-frequency z-site line. For $0>\mathrm{id}>-\frac{3}{4}$, the quadratic shift is negative for the higher-frequency y-site line. These predictions are in good agreement with the experimental results. Note that positive quadratic shifts are possible for the higher-frequency line, but

have not been seen because none of the observed shell id values are sufficiently large. Furthermore, we note that the quadratic terms in the splitting parameters are also not observed for the same reason. Finally, Eqs. (20) and (21) predict that in the linear approximation $\Delta a_z/\Delta a_y = -2$. Slope ratios near this value are seen for many shells but somewhat large deviations are also found (e.g., shell B). Inclusion of the RREF effect and higher-order stress terms does not account very well for these deviations.

In summary, by choosing an appropriate value for the id parameter and using the universal curves shown in Fig. 9, the observed-shift-versus-stress curve can be reasonably well fit. Thus, the simplified theoretical results suggest that only one parameter id is needed to account for the three experimentally measured piezohyperfine constants. The RREF effect and higher-order stress terms modify the value of the id parameter from that given in Eq. (23). However, the universality of the curve shapes obtained from Eqs. (20) and (21) are not basically changed.

B. Qualitative Results for Specific Shells

1. k_0 *Location Problem*

Before quantitative results can be calculated a choice of the Δ_1 band minimum location k_0 must be made. The original ENDOR experiment[3] found $k_0 = (0.85 \pm 0.03)k_{max}$. The results of the later experiment[4] suggested that the error limits should be larger but $0.85k_{max}$ was a reasonable average value.[15] A number of different types of optical experiments have yielded smaller values. An early optical-absorption experiment[37] found $k_0 = 0.81\ k_{max}$. Another optical experiment[38] was analyzed by Dumke[29] to yield $k_0 = 0.82k_{max}$. Results from a recent photoconductivity study[40] yield $k_0 = 0.79k_{max}$. A fourth optical experiment[41] found $k_0 = (0.76 \pm 0.06)k_{max}$. Band-structure calculations favor the mideighty values.[42] Because of these various results we have performed calculations for a range of k_0 values about $0.85\ k_{max}$.

2. *Previous Shell Assignments*

To compare the results for a given experimental shell with the theoretical predications for that shell, it is necessary to mate the actual lattice shell to the measured shell. Unfortunately, the prevailing theory is not accurate enough to match most of the shells.[15] It is known that shell A is the (0, 0, 4) shell[3]; shell K is the (0, 0, 8) shell[4]; shell B is most likely the (4, 4, 0) shell[3,43]; and shell E is the (1, 1, 1) shell. In the remainder of this section we will make a comparison with the above shells. For other shells, matchings have not been definitely established although many possibilities have been ruled out. We will consider the implications of the present data and previous results for matching these other shells.

3. *Present Results for Specific Shells*

a. From of Comparison. For comparison of the theoretical results and the experimental data we use the normalized piezohyperfine constants. This form of comparison has two advantages. One is that the comparison is between the percent changes in $|\psi|^2$. Second, dividing the shift or splitting by a_0 removes the dependence on the envelope function to first order [see Eqs. (20)–(22)].

We note that the Fermi contact interaction measures the wave-function density $|\psi|^2$ at the different lattice sites; the dipolar constants measure variations in $|\psi|^2$ in the vicinity of the particular lattice site; while the uniaxial stress experiment primarily measures changes in $|\psi|^2$ at the lattice site (Fermi contact changes only) produced by the stress. Consequently, comparisons using the Fermi contact constants[3,15] emphasized a detailed knowledge of both the radial dependence of the envelope function and the interference effects between the cosine terms of Eq. (12), i.e., $a_0 \propto (1+2R)^2$. For the dipolar constant comparisons,[16] the theory required adding a few new, but apparently reasonable assumptions to perform the calculations. The comparisons again emphasized interference effects between different expressions involving cosine terms. (In principle, the envelope function can be "normalized out.") The present normalized constant comparisons emphasize stress-induced changes between the interfering terms in Eq. (12), i.e., $(\Delta a/a_0) \propto (1-R)/(1+2R)$. Thus, the uniaxial stress experiment emphasizes a different aspect of the theory than previous comparisons. At the present time, it is difficult to judge between the relative merits of these different approaches. All three types of data are useful and none should be neglected *a priori* when considering the unsolved problem of identifying most of the shells.

b. $\langle 111 \rangle$*-axis-class shells.* Since the linear shifts are effectively zero, there is only one piezohyperfine constant for each $\langle 111 \rangle$-axis-class shell. We express this constant as C which is the best-fit constant on the range $0 > X > -\frac{1}{2}$ to the expression

$$a(X)/a(0) = |\psi(X)|^2/|\psi(X=0)|^2 = 1 - X^2/C \ . \quad (24)$$

Thus from the experimental results, $C = 2[fa(0)]^{-1}$ as a comparison of Eqs. (16) and (24) shows. The theoretical results, using only the valley repopulation model, yield for every shell of the $\langle 111 \rangle$ axis class

$$\frac{|\psi(X)|^2}{|\psi(X=0)|^2}=\frac{1}{6}\left|\sum_{j=1}^{6}\alpha_j\right|^2\approx 1-\tfrac{1}{18}X^2+\tfrac{1}{54}X^3+\tfrac{1}{216}X^4+\cdots . \quad (25)$$

This result was first obtained by Wilson and Feher[6] for the donor, which is just the $r=0$ ⟨111⟩-axis-class shell. For the donor the best fit to this expression in the range $0>X>-\frac{1}{2}$ is $C\simeq 16$, a number which is independent of donor or shell radius. Note that $C\neq 18$ because of the influence of the cubic and higher-order terms. Inclusion of the RREF effect modifies this result. The donor-dependent modifications using the Whittaker function calculations are shown for $r=0$ in Fig. 6. The radial dependence is such that an increasing r value corresponds to a slower fall off of this quantity with X. For example, the As (5, 5, 5) shell lies just below the P curve of Fig. 6. If the b^* exponential form for the wave function is used, the radial dependence of $a(X)/a(0)$ is considerably weaker. Also this quantity falls off faster as r increases out to $r\approx(\bar{7},\bar{7},\bar{7})$, beyond which the effect switches sign and behaves like the Whittaker function calculation. The results of these calculations and the experimental numbers are given in Table II. (The experimental errors are mainly due to making rather small absolute shift measurements.[44] For a given donor, the trends in the data are more significant than the error limits imply.)

The experimental results show that there is a definite donor and shell dependence of the C constants. Thus, the valley-repopulation model by itself is not adequate. The variation between shells is considerably more than the b^* exponential calculation predicts. The Whittaker function calculation is not completely adequate either, but it does predict a larger donor and shell dependence especially for an arsenic donor. These results are observed in the data. This latter calculation also predicts that larger C constants should be associated with larger r values. If this prediction is correct, clearly shell N is far out in the $(\bar{7},\bar{7},\bar{7})$, $(8,8,8)$, $(\bar{8},\bar{8},\bar{8})$, or $(9,9,9)$ group while shell H and shell O are nearer[45] in the $(\bar{3},\bar{3},\bar{3})$, $(4,4,4)$, $(\bar{4},\bar{4},\bar{4})$, or $(5,5,5)$ group. (The dipole calculations[16] also suggest that shells H and O are from the same nearby group.) Conclusions regarding shells C and J are not definitive. (The Fermi contact calculations suggest shell C is in the nearby group.)

c. Other shell classes. Calculations for shells other than the ⟨111⟩-axis-class shells are dependent on the choice of k_0.[46] For several values of k_0, theoretical calculations have been carried out for the normalized piezohyperfine splitting constants. The results are displayed in Fig. 10 for many As shells, in Fig. 11 for the P shells, and in Fig. 12 for the Sb shells. In plotting the curves, we have considered the first 126 nearest-neighbor shells ($r<16$ Å). Of these shells nine are of the ⟨111⟩ axis class with id = 0 and 57 are of the unique class, a shell class to which none of the lettered shells belong. Of the remaining sixty shells, 25 have been plotted on each graph; nine cannot be shown since their small a_0 means a very large id parameter; and 26 have not been plotted since their small a_0 value (due to their large distance from the donor) seems to exclude them from the data. The column on the right of each figure shows the measured id values for the proper donor except shells M(P) and L(P) which did not fit on the scale.

TABLE II. Piezohyperfine C constants for ⟨111⟩-axis-class shells. The theoretical constants are computed using the Whittaker (Whit.) function form and the exponential (b^*) form for the envelope function.

	As		P		Sb	
	Calc values					
Shell	Whit.	b^*	Whit.	b^*	Whit.	b^*
(0, 0, 0)	$12\frac{1}{2}$	15	14	$15\frac{1}{2}$	14	$15\frac{1}{2}$
(1, 1, 1)	$12\frac{1}{2}$	15	14	$15\frac{1}{2}$	14	$15\frac{1}{2}$
$(\bar{3},\bar{3},\bar{3})$	13	15	14	$15\frac{1}{2}$	14	$15\frac{1}{2}$
(4, 4, 4) or $(\bar{4},\bar{4},\bar{4})$	13	15	14	$15\frac{1}{2}$	14	$15\frac{1}{2}$
(5, 5, 5)	$13\frac{1}{2}$	15	$14\frac{1}{2}$	$15\frac{1}{2}$	14	$15\frac{1}{2}$
$(\bar{7},\bar{7},\bar{7})$	$14\frac{1}{2}$	$15\frac{1}{2}$	$14\frac{1}{2}$	$15\frac{1}{2}$	$14\frac{1}{2}$	$15\frac{1}{2}$
(8, 8, 8) or $(\bar{8},\bar{8},\bar{8})$	15	15	$14\frac{1}{2}$	$15\frac{1}{2}$	$14\frac{1}{2}$	$15\frac{1}{2}$
(9, 9, 9)	$15\frac{1}{2}$	15	15	$15\frac{1}{2}$	$14\frac{1}{2}$	$15\frac{1}{2}$
	Expt values					
C	$14\frac{1}{2}\pm 1$		13 ± 1		15 ± 1	
H	12 ± 2		$15\frac{1}{2}\pm 2$		$12\frac{1}{2}\pm 2$	
J	24 ± 7		$14\frac{1}{2}\pm 2$		14 ± 2	
N	21 ± 3		18 ± 4		···	
O	10 ± 3		$13\frac{1}{2}\pm 2$		$11\frac{1}{2}\pm 2$	

Consider first the matched shells A, B, and K whose matchings are emphasized by the cross-hatched circles on the figures. These circles suggest $k_0\approx 0.86k_{max}$[47] with a spread of about $0.03k_{max}$ for the same donor. This value for k_0 is consistent with the unstressed Fermi contact matchings.[3,15] However, the spread is considerably smaller than for the unstressed cases where for an arsenic donor the spread is $0.14k_{max}$. (We note that if the RREF effect is neglected the theoretical curves shift towards larger id values and yield $k_0\approx 0.89k_{max}$ with a spread of $0.04k_{max}$.) Thus, the theory is reasonably consistent in determining a k_0 value for these shells. However, as a later discussion shows, this is not always the case when the other shell matchings are considered.

The experimental results show that two other piezohyperfine parameters can be considered for each of these shells. To obtain these parameters theoretically, we plotted a number of curves for each shell, examples of which are shown in Fig. 7.

The results using this procedure normally yielded k_0 values quite near the value obtained from Figs. 10–12. Little new information was obtained. Thus, to within the accuracy of the present results, only one "theoretical" piezohyperfine parameter id needs to be considered for each shell, although three "experimental" parameters are measured for each shell. This approximate one-parameter fit indicates the universality of the curve shapes in Fig. 9 as was discussed in Sec. IV A.

The shells D, F(As, P), G, I, L, M, P, Q, R, and V(Sb) are shown on Figs. 10–12 and have not been matched. In Table III, the various possible lattice shells are shown and their id's are grouped in three categories – positive, negative, and small. They are also divided into three groups based on the magnitude of the Fermi contact hyperfine constants, i.e., the likelihood that they have been experimentally measured. The experimental shells are also shown grouped according to their id parameters.

Table III and also Figs. 10–12 indicate that the (1, 1, 5) and (1, 1, 9) shells are the best candidates for shell Q. However, the calculated Fermi contact constant of shell (1, 1, 9) is approximately a factor of 2 smaller than that of shell (1, 1, 5) which is close ($k_0 = 0.86 k_{max}$) to the experimental value for shell Q.[4] The experimental dipolar constants of shell Q [4] are also very consistent with the dipole-dipole calculations for shell (1, 1, 5).[16] Although a matching circle for shell Q and (1, 1, 5) cannot be drawn on Figs. 10–12, a small correction would make this possible. In addition, there is no other good candidate for (1, 1, 5), which is very likely to have been measured. All the present calculations and experimental results can be reconciled by assigning shell Q as (1, 1, 5).

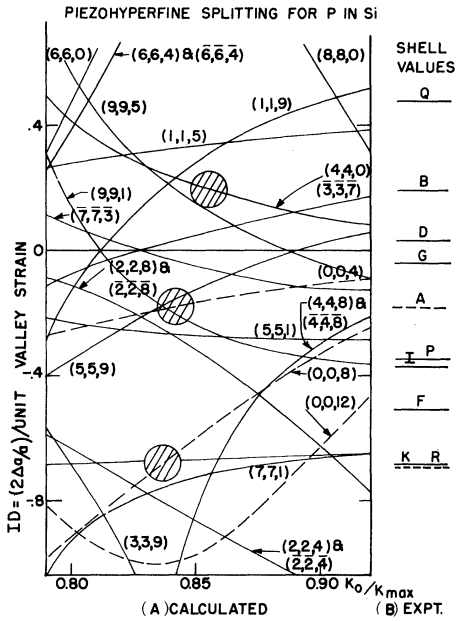

FIG. 11. Comparison of theoretical and experimental results for phosphorus shells. The cross-hatched circles show the previously matched shells. Results for the ⟨001⟩-axis-class shells are shown by dashed lines. Some of the nearby lattice shells cannot be shown on the plot (see text). Shells L(P) and M(P) could not be shown on the plot.

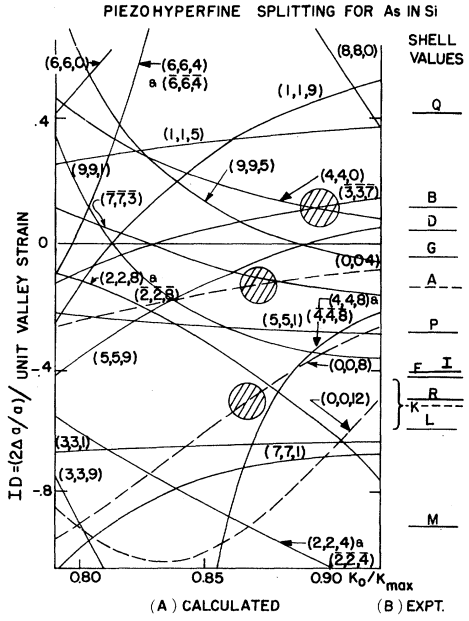

FIG. 10. Comparison of theoretical and experimental results for arsenic shells. The cross-hatched circles show the previously matches shells. Results for the ⟨001⟩-axis-class shells are shown by dashed lines. Some of the nearby lattice shells cannot be shown on the plot (see text).

Careful thought has been given to matching other shells based on the three different types of data – Fermi contact constants, dipole-dipole constants, and piezohyperfine constants. No other definite matches have been found, however several interesting features should be noted. Consider the interchanged pair of lattice shells (n, n, m) and (m, m, n), e.g., (0, 0, 4) and (4, 4, 0).[48] For one of these $R < 1$, while for the other $R > 1$. Restricting our attention to the observed shells $[(1 + 2R)$ reasonably large] one can readily show that $\mathrm{id}(n, n, m) \simeq -\mathrm{id}(m, m, n)$.[49] Figures 10–12 indicate that shells A and B satisfy this relationship and also suggest that shells D and G may constitute an interchanged pair with rather small id parameters. The observable interchanged pairs shells with very small id's are $(\bar{3}, \bar{3}, \bar{7})$-$(\bar{7}, \bar{7}, \bar{3})$ and (5, 5, 9)-(9, 9, 5), however, there are other shells which also may have small id's [e.g., (3, 3, 11), (2, 2, 12)].

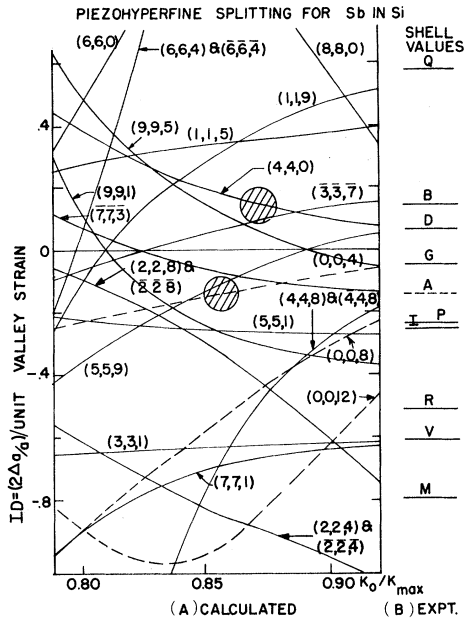

FIG. 12. Compariosn of theoretical and experimental results for antimony shells. The cross-hatched circles show the previously matched shells. Results for the ⟨001⟩-axis-class shells are shown by dashed lines. Some of the nearby lattice shells cannot be shown on the plot (see text).

The Fermi contact hyperfine constants for (5, 5, 9) and (9, 9, 5) are almost certainly too small to account for shells D and G, which exhibit relatively large values of a_0. Consideration of the Fermi contact and dipole-dipoleconstants and the id parameter reveals that $(\bar{7}, \bar{7}, \bar{3})$ is a good candidate for G; however, $(\bar{3}, \bar{3}, \bar{7})$ is only a fair candidate for D (the calculated $\frac{1}{2}a_0$ is about 30% too small; B_{zz} has the wrong sign). Despite the good fit of shell G and $(\bar{7}, \bar{7}, \bar{3})$ we suggest this only as a tentative assignment at present. Finally, we note that shell (5, 5, 1), which is the interchanged mate of shell Q, has probably been measured but has not been matched. Shell (5, 5, 1) is expected to have a larger a_0 value than (1, 1, 5), $(\bar{3}, \bar{3}, \bar{7})$, and (2, 2, 8) and is a possible candidate for shell D. Should this be confirmed it would indicate a serious discrepancy (both in sign and magnitude) between the calculated and observed id values for this shell.

Two other shells which show extremely small shifts are S(P) and T(P). (Due to overlapping complex spectra the analysis 3as only possible in P.) Both S(P) and T(P) have shifted less than 5 kc/sec at $X \approx -0.6$. T(P) is particularly remarkable because there is hardly any line broadening at $X \approx -0.6$. The shells with large enough Fermi contact constants to account for shells S and T, and yet have very small id values near $k_0 = 0.86k_{max}$, are (5, 5, 9), (9, 9, 5), and (2, 2, 12). No definite assignment of S and T is possible at present.

We have also considered the inversion related pairs, e.g., (2, 2, 8) and $(\bar{2}, \bar{2}, \bar{8})$, which the present models predict to have the same id parameters. (This is not a symmetry requirement; however, it is not known in detail how to treat this problem.) No conclusions could be reached on these inversion related pairs.

d. Relationship between B_{zz}/a_0 and id *Parameter*? Uniaxial stress applied along a cubic [001] axis makes this axis different than the other cubic axes and alters the z dependence of the wave function with respect to the (x, y) dependence. The id parameter measures the difference of the z- and y-site linear percent changes in these dependences per unit valley strain. One of the hyperfine tensor components B_{zz} measures how much the wave-function probability density in the vicinity of a particular lattice site is preferentially weighted along the z axis. This suggests the possibility of a relationship between the id parameter and the quantity B_{zz}/a_0 (zero-stress data). Employing an expression developed by Hale and Mieher[16] [Eq. (12)] and the definition of R [see Eq. (23)], one finds

$$B_{zz}/a_0 = -(I_0/A_0)[(1-R^2)/(1+2R)^2] \quad . \tag{26}$$

The quantity (I_0/A_0) has been introduced in Sec. II. Using Eq. (23), this becomes

$$B_{zz}/a_0 = -[(1+R)/(1+2R)](I_0/A_0)\text{id} \quad . \tag{27}$$

The R dependence[50] in the "slope" relating B_{zz}/a_0 and the id parameter complicates the result

TABLE III. Matching considerations for {110} -plane-class shells based on the id and a_0 values.

		Positive id	Negative id	Small id
Lattice shells	Very likely	(1, 1, 5)	(5, 5, 1)	$(\bar{3}, \bar{3}, \bar{7})$
			(2, 2, 8)	$(\bar{7}, \bar{7}, \bar{3})$
	Likely	(1, 1, 9)	(9, 9, 1)	(5, 5, 9)
			(2, 2, 4)	(9, 9, 5)
			$(\bar{3}, \bar{3}, \bar{1})$	(2, 2, 12)
	Unlikely	(6, 6, 0)	$(\bar{7}, \bar{7}, 1)$	$(\bar{3}, \bar{3}, \bar{11})$
		(10, 10, 0)	(4, 4, 8)	$(\bar{11}, \bar{11}, \bar{3})$
				(1, 1, 13)
Expt shells		Q	F(As, P), V(Sb)	D, G,
			I, L, M, P, R, X	S(P), T(P)

[a] Indicates the probability a given shell has been measured.

[b] Also $(\bar{2}, \bar{2}, \bar{8})$, $(\bar{2}, \bar{2}, \bar{4})$, $(\bar{4}, \bar{4}, \bar{8},)$ $(\bar{2}, \bar{2}, \bar{12})$, the inversion related, but not identical shells should also be considered in this table.

somewhat but Eq. (27) indicates that for most observed shells ($R<-1$ or $R>-\frac{1}{2}$) that B_{zz}/a_0 should have the opposite sign of the id parameter and should be approximately I_0/A_0 (about $\frac{1}{20}$) times the id parameter.

A plot of experimental B_{zz}/a_0 values[4] versus the experimental id for the three donors for the {110}-plane-class shells is shown in Fig. 13. The figure shows that many of the shells are approximately consistent with Eq. (27), namely, B_{zz}/a_0 has the opposite sign of the id and the magnitude of B_{zz}/a_0 increases with the magnitude of id. Shells D, I, L, M, and P fall in the wrong quadrants (B_{zz}/a_0 and id have the same sign) and are in bad agreement with Eq. (27). The explanation for this is not known. For shell D both B_{zz}/a_0 and the id are rather small and a small correction in one of the calculated quantities could account for this behavior. However, shells I, L, M, and P require sizable corrections to the present theory. It is significant that none of these deviant shells has yet been assigned to a particular lattice shell, whereas shells A, B, K, and Q, which have been matched, satisfy the relationship between B_{zz}/a_0 and id fairly well, even though K and Q show deviations outside of experimental error.

A second feature of Fig. 13 is the unusually large donor differences for shells F [V(Sb) is thought[4] to be a modified form of shell F] and L, and possibly M. [Note, however, that a 10% increase in Ξ_u for P would reduce many of these donor anomalies.] Figure 13 gives an indication of which shells show the largest deviations from present theory; however, it is difficult to ascertain the nature of the corrections. On the basis of the donor anomalies the results seem to suggest that primarily B_{zz}/a_0 needs to be corrected for shell F, while for shell L and possibly M, it is the id parameter which needs to be corrected.

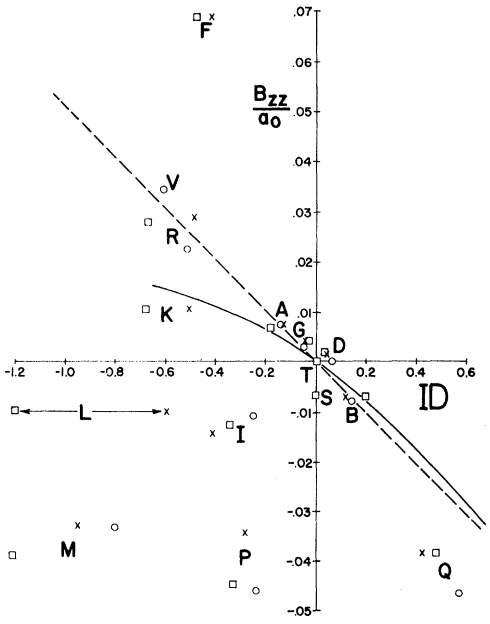

FIG. 13. Normalized zero-stress dipole-dipole constant B_{zz}/a_0 dependence on the id parameter. The solid line is the theoretical relationship based on Eq. (27) while the dashed line shows a linear relationship with slope (I_0/A_0) between B_{zz}/a_0 and id (see Ref. 50). The experimental values for As(x), P(□), and Sb(0) are also shown in the figure.

APPENDIX A: SUBDIVISION OF A SHELL INTO SETS UNDER AN APPLIED PERTURBATION

The nuclei which form a shell must transform into each other under the point group operators which leave the crystal symmetry and impurity symmetry invariant. When a perturbation is applied, such as a magnetic field, a stress, or an electric field, only certain of these operators leave the geometrical relationship between the crystal, the impurity, and the perturbation invariant. These operators form a group. The nuclei, which remain related by using only those operators of the new group, form a set of nuclei. In general, a shell divides into two or more sets depending upon the shell class and the applied direction of the perturbation.

In the present problem, a [001] axis stress changes the impurity site symmetry from T_d to D_{2d} with operators E, $3C_2$, $2\sigma_d$, and $2S_4$. A brief consideration shows that only the $3C_2$ operators are necessary to establish the equivalence of the four nuclei which form either the x, or the y, or the z sites. In addition, the equivalence of the x- and y-sites nuclei can be established by any one of the σ_d or S_4 operators. Furthermore, none of the D_{2d} operators transform any of the z sites into x or y sites. Thus, the [001] axis stress subdivides the {110}-plane-class and the ⟨001⟩-axis-class shells into two sets. One set is composed of the z sites; the other set is composed of the x and y sites. The ⟨111⟩-axis-class shells do not subdivide since the four nuclei in any one shell effectively compose a set of x sites.

The above technique may be applied with minor modifications to a case of simply a magnetic field along the [100] axis. Then, the x sites form one set; while the y and z sites form another. If a [001] axis stress is applied along with the [100] axis magnetic field, then there are three independent sets corresponding to the x, y, and z sites. Extensions of the method to other geometries is not difficult.

APPENDIX B: STRESS SHIFT FOR SMALL VALLEY STRAIN

A reasonable physical understanding of how the various ENDOR lines shift with stress can be obtained using the approximation $|X| \ll 1$. Consider the normalized shift of a z-site line given by

$$2\Delta a_z/a_0 \equiv (a_z(X) - a_0)/a_0 = a_z(X)/a_0 - 1 \qquad \text{(B1a)}$$

$$= \frac{|\psi(n,n,m;X)|^2 - |\psi(n,n,m;0)|^2}{|\psi(n,n,m;0)|^2}, \qquad \text{(B1b)}$$

where the zero subscript stands for the unstressed value and Δa_z is the shift directly measured by the experiment. Using the notation of Eq. (13) we can write

$$\frac{a_z(X)}{a_0} = \frac{6F_z^2(\vec{r},X)}{F_z^2(\vec{r},0)}\left(\frac{1+2Rf}{1+2R}\right)^2\left(\frac{\alpha_z + 2\alpha_y Rf}{1+2Rf}\right)^2, \qquad \text{(B2)}$$

where $$f \equiv F_y(\vec{r},X)P_z(\vec{r})/F_z(\vec{r},X)P_y(\vec{r}) \ , \qquad \text{(B3)}$$

$$R = \frac{P_y(\vec{r})\cos[\frac{1}{2}\pi(k_0/k_{\max})r]}{P_z(\vec{r})\cos[\frac{1}{2}\pi(k_0/k_{\max})m]} . \qquad \text{(B4)}$$

In the above $P_y(r)$ is the y-site pancake function which we assume to be independent of stress. The parameter f is in the range 1.0–1.2 for $0 > X > -\frac{1}{2}$ and would be one if the RREF effect is neglected. The location parameter R has a strong site location dependence caused mainly by the dependence of the cosine terms on the integers m and n.

Equations (7) and (8) yield for $|X| \ll 1$

$$\alpha_z = (1 - \tfrac{1}{3}X + \tfrac{1}{36}X^2 + \cdots)/\sqrt{6}$$

and $$\alpha_y = (1 + \tfrac{1}{6}X - \tfrac{1}{18}X^2 + \cdots)/\sqrt{6} \ .$$

A brief derivation retaining linear and quadratic terms in X then yields

$$\frac{2\Delta a_z}{a_0} = -\tfrac{2}{3}X\left(\frac{1-Rf}{1+2Rf}\right)U\left[1 - \tfrac{1}{4}X\left(\frac{1-2Rf-2(Rf)^2}{(1+2Rf)(1-Rf)}\right)\right] + U - 1 \ , \qquad \text{(B5)}$$

where $$U \equiv \frac{F_z^2(\vec{r},X)}{F_z^2(r,0)}\left(\frac{1+2Rf}{1+2R}\right)^2 \ ;$$

U is unity if the RREF effect is neglected and deviates from one by only a small amount.

For a y-site line,

$$\frac{a_y(X)}{a_0} = \frac{6F_z^2(\vec{r},X)}{F_z^2(\vec{r},0)}\left(\frac{\alpha_z R + \alpha_y f(1+R)}{1+2R}\right)^2 . \qquad \text{(B6)}$$

Then for $|X| \ll 1$,

$$\frac{2\Delta a_y}{a_0} = \tfrac{1}{3}X\left(\frac{1-R}{1+2R}\right)U'\left[1 - \tfrac{1}{4}X\left(\frac{1+4R+R^2}{(1+2R)(1-R)}\right)\right] + (U'-1) - \frac{4\,U'XR(1-f)}{3\,f(1+2R)} \ , \qquad \text{(B7)}$$

where

$$U' \equiv F_z^2(r,X)f^2/F_z^2(r,0)$$

and the last term is quadratic in X, since $1-f$ is proportional to X.

As discussed in the main text, the major influence of the RREF effect is to reduce the influence of the valley-repopulation effect. Consequently, for these simple illustrative calculations, we consider only the valley-repopulation effects so that $U = U' = f = 1$. Then,

$$\frac{2\Delta a_z}{a_0} = -\tfrac{2}{3}X\left(\frac{1-R}{1+2R}\right)\left[1 - \tfrac{1}{4}X\left(\frac{1-2R-2R^2}{(1+2R)(1-R)}\right)\right], \qquad \text{(B8)}$$

$$\frac{2\Delta a_y}{a_0} = \tfrac{1}{3}X\left(\frac{1-R}{1+2R}\right)\left[1 - \tfrac{1}{4}X\left(\frac{1+4R+R^2}{(1+2R)(1-R)}\right)\right], \qquad \text{(B9)}$$

and

$$\frac{2\Delta a}{a_0} \equiv \frac{2(\Delta a_z - \Delta a_y)}{a_0} = -X\left(\frac{1-R}{1+2R}\right)\left[1 - \tfrac{1}{4}X\left(\frac{1+R}{1+2R}\right)\right], \qquad \text{(B10)}$$

where Δa is the hyperfine splitting parameter. Clearly, an important parameter which can be used to distinguish between the various shells is the shell "identifier parameter" given by

$$\text{id} \equiv (1-R)/(1+2R) \ , \qquad \text{(B11)}$$

which is essentially a geometric function of the shell location. The shape of the shift-versus-strain curves is primarily determined by the size of this parameter. For example, if id = 0 (as occurs for all ⟨111⟩-axis-class shells), then both Δa_y and Δa_z shift by the same amount and quadratically with the strain. Thus, Δa is zero. For nonzero id values, the linear term is no longer zero and can obscure the quadratic term. For most shells the linear term dominates and on this simple model one expects the z-site shift to be of opposite sign and about twice the value of the y-site shift. The id parameter can become very large only because its denominator becomes small. In such cases, however, a_0 is very small and the actual shift is not abnormally large.

APPENDIX C: VALLEY-ORBIT MATRIX AND [001] AXIS STRESS

The valley-orbit matrix,[12,6] which represents the coupling between the six Δ_1 conduction-band minima, has the form given below when a uniaxial stress is applied along the z axis

$$H_{vo} = -\Delta \begin{array}{|cccccc|} \hline x & -x & y & -y & z & -z \\ X & (1+\delta) & 1 & 1 & 1 & 1 \\ (1+\delta) & X & 1 & 1 & 1 & 1 \\ 1 & 1 & X & (1+\delta) & 1 & 1 \\ 1 & 1 & (1+\delta) & X & 1 & 1 \\ 1 & 1 & 1 & 1 & -2X & (1+\delta) \\ 1 & 1 & 1 & 1 & (1+\delta) & -2X \\ \hline \end{array} \qquad \text{(C1)}$$

Δ is the coupling between adjacent valleys, $\Delta(1+\delta)$ is the coupling between opposite valleys, and the reduced valley strain X is given by $(\Xi_u/6\Delta) \times 2(S_{11}-S_{12})T$, where S_{11} and S_{12} are elastic coefficients, T is the tensile stress, and Ξ_u is the "shear" deformation potential. Bases on the deformation-potential approach (linear theory) the effect of strain is a diagonal effect only shifting the different minima up or down but not coupling the different valleys.

Because of the coupling between the valleys the sixfold degenerate states break into (T_d symmetry) a singlet A_1 state, a doublet E state, and a triplet T_2 state. Using the $\alpha_n(j)$ for these states to form a unitary matrix Eq. (C1) may be almost diagonalized (exact for $X=0$) and has the form

$$H'_{vo} = -\Delta \begin{vmatrix} A_1 & E_a & E_b & T_{2x} & T_{2y} & T_{2z} \\ (5+\delta) & \sqrt{2}X & 0 & 0 & 0 & 0 \\ \sqrt{2}X & -(1-\delta+X) & 0 & 0 & 0 & 0 \\ 0 & 0 & X-(1-\delta) & 0 & 0 & 0 \\ 0 & 0 & 0 & X-(1+\delta) & 0 & 0 \\ 0 & 0 & 0 & 0 & X-(1+\delta) & 0 \\ 0 & 0 & 0 & 0 & 0 & -2X-(1+\delta) \end{vmatrix} . \qquad \text{(C2)}$$

This matrix shows that the only state admixed into the A_1 state $[\alpha_{A_1}^{(j)} = 1/\sqrt{6}\ (1,1,1,1,1,1)]$ is the E_a state $[\alpha_{E_a}^{(j)} = 1/\sqrt{12}\ (1,1,1,1,-2,-2)]$ by the uniaxial strain. This indicates, as does (C1), that the form of the deformed ground-state wave function is $(\alpha_y, \alpha_y, \alpha_y, \alpha_y, \alpha_z, \alpha_z)$ such that $4\alpha_y^2 + 2\alpha_z^2 = 1$. One can view the deformed ground-state wave function either as an admixture of different amounts of the z-valley wave function with respect to the x- and y-valley wave function, or equivalently can think of some admixture of E_a into the A_1 state. Matrix (C2) shows that states E_b, T_{2x}, T_{2y}, and T_{2z} are not coupled by the stress and all shift linearly with stress.

Using (C1) as a Schrödinger equation, Feher and Wilson[6] have shown that the deformed state satisfies the equation

$$4\alpha_y^2 - 2\alpha_z^2 = (3x+2)\alpha_y\alpha_z \ . \qquad \text{(C3)}$$

Using this result and the normalization condition Feher and Wilson[6] show for the deformed ground state that α_z and α_y are given by Eqs. (7) and (8), respectively.

*Work supported by the U. S. Atomic Energy Commission.

†Present address: University of Missouri, Rolla, Mo. 65401.

[1]For a review of this subject, see W. Kohn, in *Solid State Physics*, edited by F. Seitz and D. Turnbull (Academic, New York, 1957), Vol. 5.

[2]G. Feher, Phys. Rev. 103, 834 (1956).

[3]G. Feher, Phys. Rev. 114, 1219 (1959).

[4]E. B. Hale and P. L. Mieher, Phys. Rev. 184, 739 (1969).

[5]H. Fritzsche, Phys. Rev. 115, 336 (195); 120, 1120 (1960).

[6]D. K. Wilson and G. Feher, Phys. Rev. 124, 1068 (1961).

[7]D. K. Wilson, Phys. Rev. 134, A265 (1964).

[8]J. H. Reuszer and P. Fisher, Phys. Rev. 135, A1125 (1964).

[9]R. L. Aggarwal and A. K. Ramdas, Phys. Rev. 137, A602 (1965).

[10]R. E. Pontinen and T. M. Sanders, Jr., Phys. Rev. 152, 850 (1966).

[11]W. E. Krag, W. H. Kleiner, and H. J. Zeiger, Solid State Research Report No. 4, Lincoln Laboratory, MIT, 1967 p. 31.(unpublished); *ibid.* No. 1, 1968, p. 34 (unpublished) p. 34.

[12]P. J. Price, Phys. Rev. 104, 1223 (1956).

[13]C. Herring, Bell System Tech. J. 34, 237 (1955).

[14]H. Fritzsche, Phys. Rev. 125, 1560 (1962).

[15]E. B. Hale and R. L. Mieher, Phys. Rev. 184, 751 (1969).

[16]E. B. Hale and R. L. Mieher, Phys. Letters 29A, 350 (1969); Phys. Rev. (to be published).

[17]W. Kohn and J. M. Luttinger, Phys. Rev. 97, 1721 (1955); 98, 915 (1955).

[18]C. Kittel and A. H. Mitchell, Phys. Rev. 96, 1488 (1954); M. Lampert, *ibid.* 97, 352 (1955).

[19]The values for the numerical parameters used in Eqs. (3) and (4) are $a^* = 21.0$ Å, $a_t = 25.0$ Å, $a_l = 14.2$ Å, $E_0 = -29$ meV, $n(\text{As}) = 0.736$, $n(\text{P}) = 0.800$, and $n(\text{Sb}) = 0.826$.

[20]J. Bardeen and W. Shockley, Phys. Rev. 80, 72 (1950).

[21]C. Herring and E. Vogt, Phys. Rev. 101, 944 (1956).

[22]The values for these parameters can be obtained from optical data (Ref. 23). From this data, we obtained $\Delta = 3.727$, 2.16, 2.023 meV; $\delta = -0.184$, -0.308, -0.586; $\Lambda = 6.56$, 6.18, 4.58 meV for arsenic, phosphorus, and antimony donors, respectively. [The last constant Λ (Ref. 8) is the self-valley interaction parameter and is important for calculations associated with Eq. (9).] Since these parameters vary with impurity, they are sometimes called the chemical shift parameters.

[23]R. L. Aggarwal and A. K. Ramdas, Phys. Rev. 140, A1246 (1965).

[24]E. B. Hale, Bull. Am. Phys. Soc. 14, 394 (1969); (to be published).

[25]In the original work (Ref. 14), $n = n(X)$ was used to define an effective Bohr radius which varied with stress. This procedure is valid in the large r asymptotic limit. Using modern day computers, we can keep the fundamental definition as a Whittaker function index which varies with stress.

[26]The ratio B_{zz}/a_0 is also of order (I_0/A_0). The ratio is increased or decreased with respect to this value within a range of about an order of magnitude by the combination of cosine terms (also see Fig. 13).

[27]T. G. Castner, Jr., and A. M. Doyle, Rev. Sci. Instr. 39, 1090 (1968).

[28]Since we have not experimentally determined the complete hyperfine tensors for any set, we are effectively assuming that the stress changes are only in the Fermi contact term. To determine the complete tensor requires a major experimental modification in our cavity and its geometric relationship to the magnetic field. There are several substantial reasons why we believe our assumption is valid. First, the theoretical calculations show that the Fermi constants should change as experimentally observed; second, they show, in addition, that to within our experimental accuracy the stress changes in the dipolar constants should be barely detectable; finally, the experiment shows that the several dipolar constants for each shell which can be measured by rotation about the stress axis barely change if at all. Thus, it is very remote that the observed changes are not primarily in the Fermi contact constants themselves.

[29]This value is extrapolated to 30 °K.

[30]These results for $r = 0$ have actually been extrapolated from calculations for r approaching zero.

[31]F. J. Morin, T. H. Geballe, and C. Herring, Phys. Rev. 101, 525 (1957).

[32]J. E. Aubrey, W. Gubler, J. Henningsen, and S. H. Koening, Phys. Rev. 130, 1667 (1963).

[33]K. J. Schmidt-Tiedemann, in *Proceedings of the Seventh International Conference on Physics of Semiconductors, Exeter*, 1962 (The Institute of Physics and The Physical Society, London, 1962), p. 191.

[34]I. Goroff and L. Kleinman, Phys. Rev. 132, 1080 (1963).

[35]I. Balslev, Phys. Rev. 143, 636 (1966).

[36]For reasons of theoretical consistency, perhaps one donor-independent value of Ξ_u should have been chosen in some manner. In any case, if better methods become available for an absolute calibration of Ξ_u it is a simple matter to appropriately scale the experimental data given in Table I.

[37]G. G. Marfarlane, T. P. McLean, J. P. Quarrington, and V. Roberts, Phys. Rev. 111, 1245 (1958).

[38]J. R. Haynes, M. Lax, and W. F. Flood, J. Phys. Chem. 8, 392 (1959).

[39]W. P. Dumke, Phys. Rev. 118, 938 (1960).

[40]A. Onton, Phys. Rev. Letters 22, 288 (1969).

[41]R. C. Enck and A. Honig, Phys. Rev. 177, 1182 (1969).

[42]J. C. Phillips (private communication).

[43]The matching of shell *B* and (4, 4, 0) (Ref. 3) is strongly supported by the present data.

[44]Inspection of Fig. 4 shows that at $X \approx -0.54$ a shift of approximately 20 kHz for shell *C*, but only about 5 kHz for shells, *J*, *N*, and *O* which is the order of the linewidth (which has broadened from the zero stress value). This accounts for the large errors shown in Table II.

[45]The (1, 1, 1) shell is shell *E* and is not a possible candidate.

[46]For the ⟨111⟩-axis-class shell calculations, the cosine term in Eq. (13) is the same in every valley. Thus, in the normalized form of the *C* constant, there is no k_0 dependence.

[47]The smaller k_0 values for the phosphorus donor are possibly associated with the larger deformation potential for this donor (see Sec. III C 3).

[48]It can be shown that for all odd shells there is an interchanged shell; however, for many even shells there is not an interchanged shell [e.g., (2, 2, 0) or (2, 2, 4)].

[49]Note how all these interchanged pairs cross at id $= 0$ in agreement with the id $(n, n, m) \approx -$ id (m, m, n).

[50]One of us (TGC) has calculated B_{zz} employing Bloch functions rather than the equivalent orbital technique of Hale and Mieher (Ref. 16). An additional term of the form $B_{zz}/a_0 = -(I_0'/A_0)[R/(1+2R)]$ id with the integral I_0' being of similar form and about the same magnitude as I_0 has been found. For $I_0' \simeq I_0$ the addition of this extra term to Eq. (27) yields $B_{zz}/a_0 \simeq (I_0/A_0)$ id, namely, B_{zz}/a_0 should be linear in the id parameter. This result is shown by the dashed line in Fig. 13.